

**Christian Brown**

Physical Characteristics of the Nuclear Region of NGC 4388

**Faculty Sponsor**

Dr. Francisco Muller Sanchez



## Abstract

Several observed relationships between black holes and galaxies show that growth of supermassive black holes relates to galaxy evolution. These relations can be addressed by studying feeding and feedback. The KONA survey observed the core region of the Seyfert 2 galaxy NGC 4388 in the near-IR spectrum (1.963-2.379  $\mu m$ ). The OSIRIS IFS produced a datacube of a 3.3" x 4.7" region containing the AGN. Gaussian curves were fitted to the peaks of Si VI, H<sub>2</sub> 1-0 S(1), and Br $\gamma$  with QFitsView. QFitsView and Astropy were then used to produce, mask, and smooth the flux, velocity, and dispersion maps for the peaks. The Si VI and Br $\gamma$  maps showed evidence of an outflow in the south, while H<sub>2</sub> 1-0 S(1) showed evidence of a warped disk, rotation, and behavior linked to the torus. Behavior of Si VI and Br $\gamma$  in the north is likely linked to a ram pressure stripping event.

## Introduction

The most powerful and luminous objects in the known universe, supermassive black holes (SMBH) reside at the center of galaxies and can measure up to billions of solar masses. Many observed relationships between black holes and their host galaxies indicate a close connection between the formation of the two (Heckman & Best 2014). Understanding the behavior and structure of the material in the central regions of Seyfert galaxies is undoubtedly critical to the understanding of the nature of these objects due to their incredible influence on the material. Certain phenomena such as inflows and outflows are especially important to discerning an accurate description of galactic nuclei and how the material in them interacts with the SMBH. This, in turn, would also shed light on the nature of the coevolution of galaxies and SMBHs.

The Keck OSIRIS Nearby AGN (KONA) survey (Müller-Sánchez et al.), which sought to study the nuclear kinematic structure of 40 nearby active galaxies through the Keck Telescope and OSIRIS near-infrared integral field spectrograph, was conducted with the goal of researching several of these Seyfert galaxies. NGC 4388 is one galaxy observed in this survey. It is a barred spiral galaxy that is almost edge on in its inclination ( $i \approx 78^\circ$ ) (Veilleux et al.). It is a Seyfert 2 galaxy located in the Virgo Cluster (Phillips et al.) with a redshift  $z = 0.00842$  (Lu et al.). It is near the center of the cluster and one of the brightest in the cluster with a magnitude of  $M_r = -20.1$ .

The galaxy has an active galactic nuclei (AGN) and shows evidence of a very extended emission line region (VEELR) that reaches to roughly 35 kpc to the northeast of the galactic plane (Yoshida et al.). This is possibly due to past interactions with other galaxies. Evidence of a ram pressure stripping event around 200 Myr ago that pulled material off of the galaxy adds credibility to this scenario (Vollmer et al.).

There is kinematic evidence for a misaligned nuclear disk near the core of the galaxy (Greene et al.). This disk in the central  $1^\circ$  is misaligned by  $15^\circ$  from the main disk of the galaxy. Additionally, there is a maser disk, or source of a high level of stimulated spectral line emission, on the sub-pc scale (Braatz et al.). The galaxy shows uniform rotation in the  $H_2$  spectrum in the plane of the galaxy, but Bry and Si VI do not show this behavior (Greene et al.).

## Observations and Methods

The KONA survey utilized the Keck observatory in Hawaii with the OSIRIS integrated field spectrometer (IFS) to observe NGC 4388 in the near-IR spectrum (1.963-2.379  $\mu m$ ). The observation was done on December 15,

2016, with a scale of 0.05 arcsec/pixel. A region of 66 x 94 pixels was observed. The observation was done under good atmospheric conditions with an airmass of 1.15. The collected data was stored in a .fits file datacube.

QFitsView was utilized to analyze the datacube. The emission peaks for Si VI, H<sub>2</sub> 1-0 S(1), and Br $\gamma$  were identified for spectra at several different locations. Gaussian peaks were then fitted to these peaks. QFitsView was then used to automatically produce flux, velocity, and dispersion maps for these emissions centered on the wavelengths of these peaks at the central location. QFitsView produced flux maps based on the intensity of the peak at each pixel, velocity maps based the shift in wavelength of the center of the peak from the wavelength at the central position, and dispersion maps measured the full width at half maximum (FWHM) of the peak at each location. The starting parameters for Si VI were a center of 1.978187  $\mu\text{m}$  and FWHM of 130 km/s for Si VI, 2.137739  $\mu\text{m}$  and 230 km/s for H<sub>2</sub> 1-0 S(1), and 2.182589  $\mu\text{m}$  and 190 km/s for Br $\gamma$ .

The Astropy package in Python (Robitaille et al.) was then used to analyze the maps produced by QFitsView. Noise was filtered out by first removing pixels with unusually high or low values that did not fit into any physical structure. This was done by masking the maps with themselves in certain regions and choosing minimum and maximum values that were automatically replaced with a low value, 1 for velocity and dispersion maps and 0.01 for flux maps. A Gaussian smoothing function was applied to the maps and then another mask was applied using a smoothed continuum image to remove further noise in the extremes of the image. Flux maps were then normalized to the brightest pixel in each map. A rotational model was then produced for velocity maps with rotational motion. The model is in the form

$$V_{los} = \sqrt{\frac{R^2 GM}{(R^2 + A^2)^{\frac{3}{2}}}} \frac{\sin(i) \cos(\psi - \psi_0)}{\left(\cos^2(\psi - \psi_0) + \frac{\sin^2(\psi - \psi_0)}{\cos^2(i)}\right)^{\frac{3}{4}}}$$

where  $R$  is the radial coordinate,  $\psi$  is the angular coordinate,  $V_{los}$  is the velocity in the line of sight of the observer,  $G$  is the gravitational constant,  $i$  is the inclination,  $M$  is mass,  $A$  is the correspondent scale length to  $R$ , and  $\psi_0$  is the angular tilt of the plane. The velocity maps were then subtracted from this model to create residuals.

# Results

Location peak (x, y)	Flux	Height	Center	FWHM
<b>(12, 60)</b>				
Si VI	118.509	0.839419	1.448645	132.629
H <sub>2</sub> 1-0 S(1)	399.924	1.70203	58.68266	220.738
Bry	120.078	1.02774	23.37855	109.761
<b>(21, 60)</b>				
Si VI	186.494	1.11297	-21.46072	157.417
H <sub>2</sub> 1-0 S(1)	334.757	1.35027	71.83225	232.903
Bry	115.336	0.583478	4.66206	185.747
<b>(28, 71)</b>				
Si VI	172.653	1.11093	-13.7718	146
H <sub>2</sub> 1-0 S(1)	142.555	0.473062	3.049578	283.094
Bry	158.197	0.481341	-11.88695	308.755
<b>(33, 60)</b>				
Si VI	2556.6	18.3413	0.00070061	130.948
H <sub>2</sub> 1-0 S(1)	1089.83	4.34282	-5.151806	235.752
Bry	942.452	4.7224	0.07014403	187.484

Location peak (x, y)	Flux	Height	Center	FWHM
<b>(36, 49)</b>				
Si VI	527.624	1.98357	40.91657	249.888
H <sub>2</sub> 1-0 S(1)	99.2693	0.419417	-8.000039	222.349
Bry	124.587	0.538189	48.8313	217.473
<b>(41, 37)</b>				
Si VI	260.25	0.799837	-63.60072	305.673
H <sub>2</sub> 1-0 S(1)	68.0861	0.226325	-73.91846	282.614
Bry	164.192	0.315791	-74.13898	488.448
<b>(45, 60)</b>				
Si VI	1184.33	2.59361	-18.04886	428.98
H <sub>2</sub> 1-0 S(1)	159.004	0.683473	-46.06937	218.552
Bry	120.058	0.431776	-13.00337	261.217
<b>(54, 60)</b>				
Si VI	1399.58	2.78901	-101.4793	471.429
H <sub>2</sub> 1-0 S(1)	513.729	1.84718	-58.95029	261.273
Bry	90.5817	0.267641	-50.87357	3917.947

**Table 1.** Results from Gaussian fits of Si VI, H<sub>2</sub> 1-0 S(1), and Bry peaks at the given locations in velocity space. Each velocity space is centered on the wavelength of the peak at the central region.

Utilizing QFitsView, spectra were extracted from several regions of the galaxy. A diagram of this is shown in Figure 1. The following peaks were visible in the spectra:  $H_2$  1-0 S(3), Si VI, He I,  $H_2$  1-0 S(2),  $H_2$  1-0 S(1), Bry, Ca VIII,  $H_2$  1-0 S(0). The central spectra shows a slope near 0 with very prominent, narrow emission lines. Moving away from the center, the spectrum shows a more negative slope. The individual peaks of Si VI,  $H_2$  1-0 S(1), and Bry, were analyzed at these locations as well, with Gaussian curves being fitted to these peaks. The results are shown in Figures 2, 3, and 4, with the results of the Gaussian fits being shown in Table 1.

The Si VI peak broadens to the east and south sections of the map. It shows a tail of blueshift north of the AGN and slightly to the west. Slightly south of the core shows a redshifted behavior while further south shows blueshift.

$H_2$  1-0 S(1) shows redshift to west and blueshift to the east. There is some visible broadening to the north and east portions of the map. The  $V/\sigma$  map has very low values, with a maximum of around 0.4, but does grow in magnitude towards the eastern and western extremes.

Bry shows strong broadening to the south and east as well as some redshift slightly south of the nucleus. Much of the behavior far from the core may be due to atmospheric noise.

Finally, QFitsView was used to produce flux, velocity, and dispersion maps by automatically analyzing the intensity, redshift, and full width at half maximum (FWHM) of the peak at each pixel in the observed region.

Once Astropy was utilized to mask and smooth the maps, and normalize the flux maps, they were plotted as images.

The Si VI flux map shows an extremely bright center with some spots of high intensity throughout the disk, but none of these show a flux higher than 0.16. The velocity map shows very little motion in the disk, but some slight blueshift north of the disk, and an area of noticeably high redshift to the south and very high blueshift further south and slightly east. The dispersion map shows an area of dispersion over 400 km/s south of the AGN as well as areas of lower dispersion to the northwest.

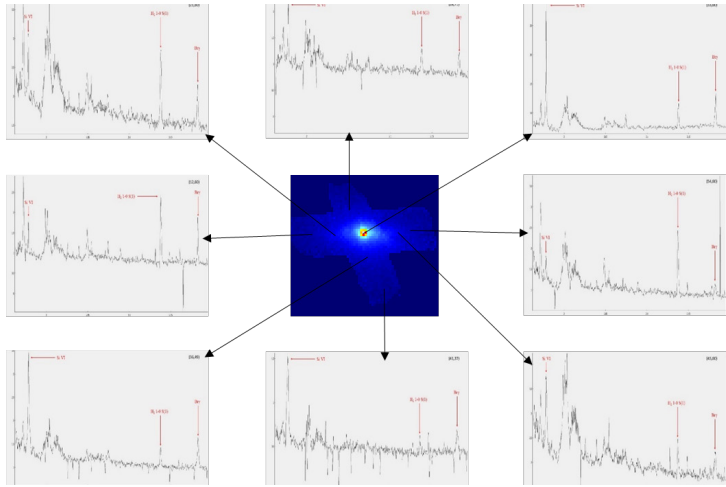


**Figure 1.** A continuum image of the galaxy (center), with spectra from the following positions (starting top right and going clockwise. Coordinates relative to center in form of (R.A., Dec.)): (0", 0"), (1.05", 0), (0.6", 1.05"), (-0.4, -1.15), (-0.15", -0.55), (-0.6", 0"), (-1.05", 0"), (0.25", 0.55"). Each spectrum shows the region (1.963-2.195  $\mu\text{m}$ ) and was extracted from a region with a pixel radius of 3. The peaks for Si VI, H<sub>2</sub> 1-0 S(1), and Br $\gamma$  are labeled on each spectrum.

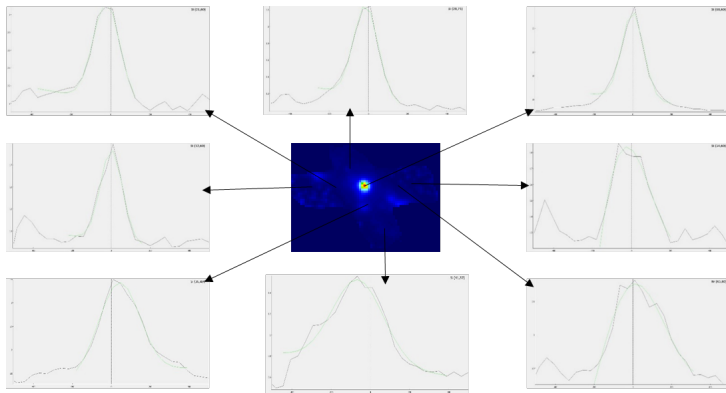


**Figure 2.** Same alignment as Figure 1 but showing the flux map for Si VI in the center and the spectrum peak for Si VI at each location. The spectra are in velocity space from -500 to 500 km/s, centered at 1.978187  $\mu\text{m}$ . A dotted line is shown on each spectrum to indicate this central position. Each peak is also shown with an approximate Gaussian fit.

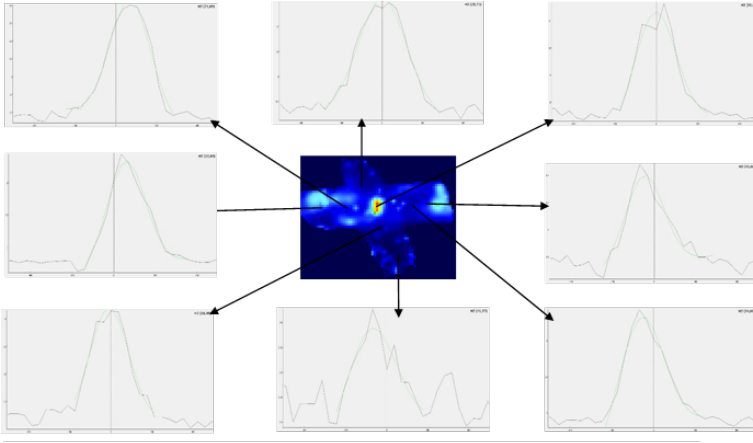


**Figure 3.** Same as Figure 2 but showing  $H_2$  1-0 S(1) flux map and spectra peaks, centered at  $2.137739 \mu m$ .

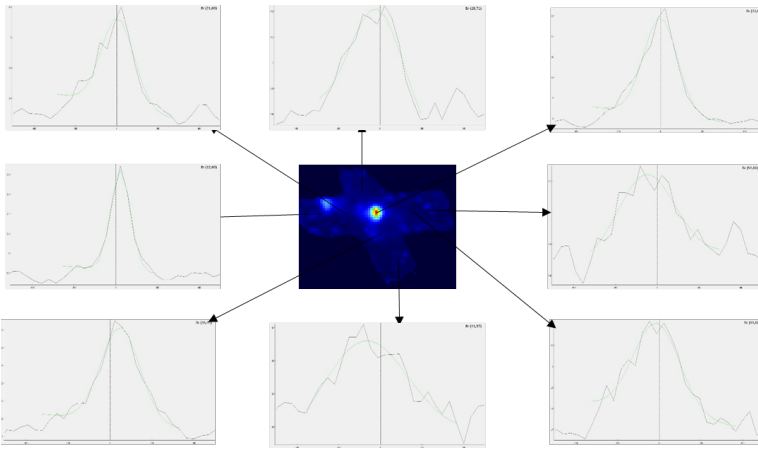


**Figure 4.** Same as Figure 2 but showing  $Br\gamma$  flux map and spectra peaks, centered at  $2.182589 \mu m$ .

The  $H_2$  1-0 S(1) flux map has a bright center, and areas of high flux within the disk both to the west and far east. The velocity map reveals a clear gradient in the disk from redshift in the west to blueshift in the east, along with some areas of slight blueshift to the far south. The dispersion map reveals spots of high dispersion scattered throughout the disk that seem to be spatially coincident with areas of low flux.

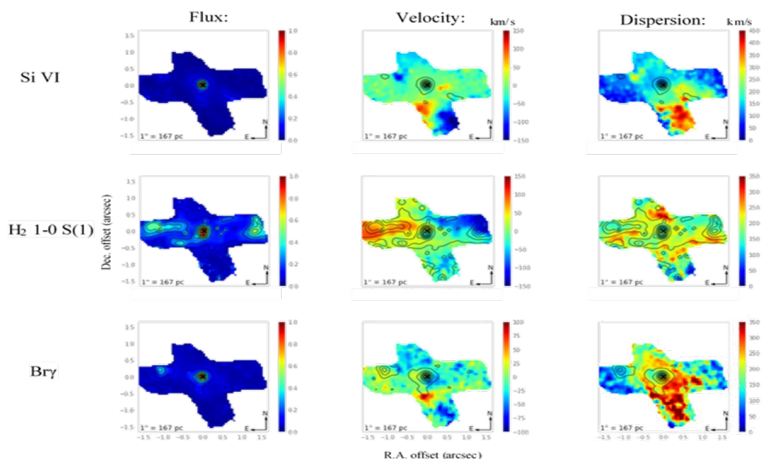


**Figure 5.** Flux, velocity, and FWHM dispersion maps for Si VI, H<sub>2</sub> 1-0 S(1), and Bry. All maps are plotted with the contours from that peak's flux map, with contours ranging from 0 to 1 on intervals of 0.1. A black x marks the estimated location of the AGN.

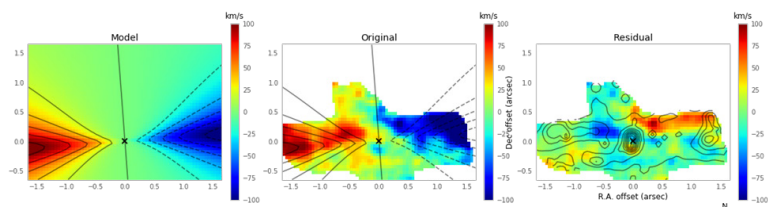


**Figure 6.** Shown are the model (left), H<sub>2</sub> 1-0 S(1) velocity map with contours of the model overlaid (center), and the residual with contours of H<sub>2</sub> 1-0 S(1) flux overlaid. The bottom section of the maps was cut to remove data that was not part of the rotational structure.

The velocity map shows similar structure to Si VI with relatively little activity in the disk, but a slight blueshift in the north, with an area of higher redshift to the south and high blueshift further southeast. The dispersion map has a ring-shaped structure of high dispersion surrounding the nucleus with extremely high dispersion in the south.

The Bry flux map has a bright center with another small area of high intensity to the west. The velocity and dispersion maps are very similar to those of Si VI but with a lower magnitude. There is also slightly more evidence of motion and dispersion within the galaxy plane.

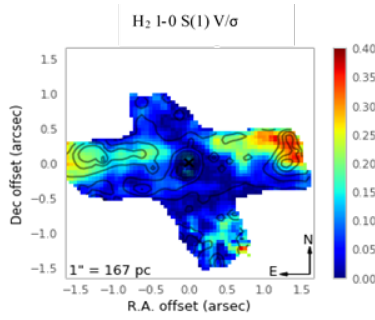


**Figure 7.** A map of the ratio of velocity and sigma for  $H_2$  1-0 S(1) overlaid with the same  $H_2$  1-0 S(1) flux contours as figure 5.

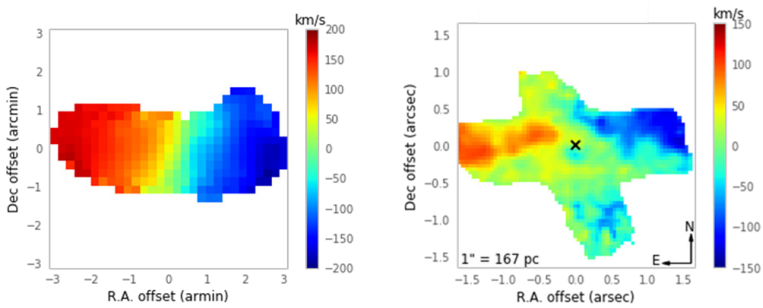


**Figure 8.** On the left is a velocity map from VIVA on the kiloparsec scale of NGC 4388. On the right is the KONA  $H_2$  1-0 S(1) velocity map on scale of 10's of parsecs. The angle of rotation for the inner area is measured to be around 82 degrees from south for the VIVA image and approximately 96 degrees from south on the KONA map. A black line has been added tracing the angle of rotation for each.

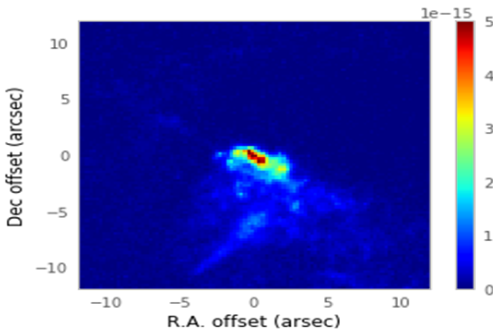


**Figure 9.** A Hubble Space Telescope image showing the OIII flux of NGC 4388. The ionization cone south of the nucleus is clearly visible.

A kinematic model in the form of

$$V_{los} = \sqrt{\frac{R^2 GM}{(R^2 + A^2)^{\frac{3}{2}}}} \frac{\sin(i) \cos(\psi - \psi_0)}{\left(\cos^2(\psi - \psi_0) + \frac{\sin^2(\psi - \psi_0)}{\cos^2(i)}\right)^{\frac{3}{4}}}$$

was created with values of  $A = 300$  pc,  $M = 2.5 \cdot 10^9 M$ , and  $i = 0.075$  radians. These values were estimated using a X2 minimization. The center of rotation is placed on the location of the AGN, and the maximum velocity within our domain is 107.5 km/s. The  $H_2$  1-0 S(1) velocity map was then subtracted from this model to produce a residue. These results are shown in Figure 7.

## Discussion

The position of the AGN was determined via level of intensity. Each continuum and flux map consistently showed the most luminous pixel in the center to be located at pixel (33, 60).

The  $\text{H}_2$  1-0 S(1) velocity map shows strong evidence of rotation in the plane of the galaxy. This is consistent with observations done on larger scales, as well as stellar rotation (Greene et al.). However, this rotation is at a different angle from rotation at larger scales. Figure 8 shows an image from VIVA (Chung et al.) on the kiloparsec scale compared to one of our images and clearly shows an offset of around 14 degrees between the two images. This offset disk has been suggested by past observations (Greene et al.).

The  $V/\sigma$  map for  $\text{H}_2$  1-0 S(1) shows relatively low values, indicating a thick disk. This combined with the aforementioned misaligned disk of rotation suggest it is aligned with the maser disk. Thus, the behavior of  $\text{H}_2$  is associated with the torus.

The maps of Si VI and Bry show evidence for strong behavior south of the galactic plane. The dispersion for both is extremely high in this region, with Si VI having dispersion above 400 km/s at some spots. The velocities of both also show strong behavior in this region, with both having an area of high redshifted velocity and blueshifted in similar regions. Bry does show high areas of dispersion around the nucleus that Si VI does not, showing it may be more prevalent in the disk of the galaxy. These observations are consistent with results from observations on slightly larger scales (Greene et al.). The motion of Si VI and Bry indicate the ionized gas in the south of NGC 4388 is likely due to an outflow. Paired with the observations of a radio jet and ionized gas south of the galaxy (Falcke et al.), this indicates the presence of an outflow from the AGN. The ionization cone can be seen in Figure 9.

The  $\text{H}_2$  1-0 S(1) velocity and dispersion maps, while weaker, also show some activity in the south with the velocity being blueshifted and dispersion showing spots of high activity. This could be evidence that some molecular gas is also involved in the outflow.

The northern section of the maps do not show as much activity as the southern part. This is due in part to some of the region being removed during the masking process due to noisy data. However, it still does show a slight blueshift in the Si VI and Bry velocity map. The dispersion maps for these two peaks also show some mild activity, while the  $\text{H}_2$  1-0 S(1) dispersion map shows a spot of high activity in this region. Such behavior does not seem to be consistent with what is occurring in the south of the galaxy. A likely explanation for this is a ram pressure stripping event. It has already been shown that NGC 4388 likely went through such an event around 200 Myr

ago (Vollmer et al.). The effects of this event are likely tied to the behavior seen in the north of NGC 4388.

## Conclusions

Data analysis of NGC 4388 revealed several things. The previously observed ionization cone and radio jet at the south of the galaxy is likely the result of an outflow from the AGN. This is most clearly seen in the dispersion and velocity maps of Si VI and Br $\gamma$ , with some possible molecular gas also present as seen in the velocity and dispersion maps of H $_2$  1-0 S(1). The H $_2$  1-0 S(1) velocity map shows clear evidence of rotation within the disk of NGC 4388. However, this does not appear to be pure rotation. The angle of rotation does not line up with the angle seen from observations of the galaxy on larger scales. This is strong evidence for a warped disk in the inner region. The small values of H $_2$  1-0 S(1)  $V/\sigma$  near the center suggest H $_2$  behavior is associated with the torus. Small blueshifted motion and low-level dispersion in the north of the galaxy are likely the result of NGC 4388 undergoing a ram pressure stripping event at some point in the past.

## References

- Braatz, J. A. et al. "A Green Bank Telescope Search for Water Masers in Nearby Active Galactic Nuclei." *The Astrophysical Journal* 617.1 (2004): L29–L32. Crossref. Web.
- Chung, Aeree et al. "Erratum: 'VLA Imaging of Virgo Spirals in Atomic Gas (Viva). I. The Atlas and the HI Properties.'" *The Astronomical Journal* 139.6 (2010): 2716–2718. Crossref. Web.
- Greene, Jenny E. et al. "Circumnuclear Molecular Gas in Megamaser Disk Galaxies NGC 4388 and NGC 1194." *The Astrophysical Journal* 788.2 (2014): 145. Crossref. Web.
- Heckman, Timothy M. and Best, Philip N. "The Coevolution of Galaxies and Supermassive Black Holes: Insights from Surveys of the Contemporary Universe." *Annual Review of Astronomy and Astrophysics* 52.1 (2014): 589-660. Crossref. Web
- Falcke, Heino, Andrew S. Wilson, and Chris Simpson. "Hubble Space Telescope and VLA Observations of Seyfert 2 Galaxies: The Relationship Between Radio Ejecta and the Narrow-Line Region." *The Astrophysical Journal* 502.1 (1998): 199–217. Crossref. Web.
- Lu, N. Y., Hoffman, G. L., Groff, T., Roos, T., Lamphier, C. "H i 21 Centimeter Observations and I-Band CCD Surface Photometry of Spiral Galaxies behind the Virgo Cluster and toward Its Antipode." *Astrophysical Journal Supplement* v.88 (1993): 383-413. Crossref. Web.
- Müller-Sánchez, F. et al. "The Keck/OSIRIS Nearby AGN Survey (KONA). I. The Nuclear K-Band Properties of Nearby AGN." *The Astrophysical Journal* 858.1 (2018): 48. Crossref. Web.
- Phillips, M.M. and Malin, D.F. "NGC 4388: a Seyfert 2 galaxy in the Virgo cluster." *Mon. Not. R. Astr. Soc.* 199.4 (1982) 199, 905-913. Crossref. Web.
- Robitaille, T. P. et al. "Astropy: A community Python package for astronomy." *A&A* 558, A33 (2013): 1432-0746. Crossref. Web.

- Veilleux, S., J. Bland-Hawthorn, and G. Cecil. "A Kinematic Link Between Boxy Bulges, Stellar Bars, and Nuclear Activity in NGC 3079 and NGC 4388." *The Astronomical Journal* 118.5 (1999): 2108–2122. Crossref. Web.
- Vollmer, B. et al. "Two Uneven Sisters." *Astronomy & Astrophysics* 620 (2018): A108. Crossref. Web.
- Yoshida, Michitoshi et al. "Discovery of a Very Extended Emission-Line Region Around the Seyfert 2 Galaxy NGC 4388." *The Astrophysical Journal* 567.1 (2002): 118–129. Crossref. Web.

Daniel Duong completed his B.S. in physics from the University of West Florida in August 2019. He was a member of the Society of Physics Students as well as the head of media for the Baptist Collegiate Ministries. Daniel was also involved in computation physics research under Dr. Christopher Varney. Over the summer of 2018, Daniel received an opportunity to conduct research under Dr. Firouzeh Sabri at the University of Memphis through the Research Experience for Undergraduates program funded by the National Science Foundation.

**Daniel Duong**  
The Synthesis and Preparation of Upconverting and  
Downconverting Phosphors for Sensing Applications

**Faculty Sponsor**  
Dr. Firouzeh Sabri

## Introduction

Thermometry has always been important for scientific and industrial applications. Its usage ranges from environment sensing and climate control to medical uses. Thermometry plays an important role in determining if a region of space is suitable to the application at hand, from habitable conditions and possible hazards to the usage of electronics. It helps determine how certain materials will behave, thus informing the best way to prepare accordingly.

Just as the applications of thermometry have a wide array, so are the types of thermometry, each with their respective strengths and weaknesses. One type of thermometry uses thermal expansion. A classic example of this would be the mercury thermometer. The mercury expands as it is heated, and the volume is then used to determine the temperature. While useful for a broad range of applications, a downside is that it must be in contact with the material itself. Other types of thermometry require a medium to travel through, are not highly accurate, or cannot detect a wide range of temperatures (Aryal, 2018). For the purposes of space exploration and settlement, these factors play a significant role in determining the type of thermometry used. As a result, phosphor thermometry is a strong contender to be the best way to deal with these issues.

Phosphor thermometry operates by using photoluminescence, thus avoiding all of the issues above. This occurs by shooting a short pulse laser at the phosphor, enabling the electrons to reach an excited state, and measuring the emissions from the electrons as they fall back to ground level (Aryal, 2018). This is why the phosphors are described as upconverting and downconverting. For the purposes of this experiment, the decay rate will be used to determine the temperature, as it is the most widely-used method, and a method which is compatible with a configuration which will be stated later (Allison et al, 2017). Phosphor thermometry does have one weakness, however. The phosphors are in powder form, which makes them difficult to handle.

Due to their small particle size, a variety of issues arise. They will easily cross contaminate with other materials, messing up measurements. In addition, their high surface charge causes them to adhere to most materials as well as cluster together, creating a non-uniform amount of the powder for sensing. Outside forces will cause the powder to disperse. In this form, the phosphor powders are hazardous, not only to people, but also to the environment, therefore necessitating Environmental Protection Agency regulations. Lastly, the phosphors are reusable, but not recoverable in this state, and can only be utilized on a limited number of surfaces (Rietema, 1991). Thus, the proposed

solution is to encapsulate the powders in Sylgard 184.

Sylgard 184 is classified under the family of polydimethylsiloxane (PDMS). PDMS is a common elastomer used for space exploration due to its insulating abilities, flexibility, non-flammability, and easy synthesis. Especially critical in this experiment is PDMS's characteristic of being inert (Fontenot et al, 2016). This allows it to be doped with different materials, enabling the creation of composites. By forming a composite with the phosphor powders, the phosphor itself becomes easier to handle and thus, more applicable. PDMS is also transparent in the visible spectrum, thereby not distorting the photoluminescence of the phosphor powders (Allison et al, 2017).

The purpose of this experiment is to create a method in which the phosphor powders can be reliably encapsulated without the loss of the powder. In addition, the identification of the best suited temperature dependent bandwidths will be identified. Finally, an investigation was made to see if the encapsulation process had any effect on the excitation or emission behavior of each compound.

## **Materials**

Thirteen different phosphor powders were acquired for this research. Eight of the powders were acquired from Intelligent Materials, and the other five were acquired from the University of Louisiana, Lafayette. The powders acquired from Intelligent Materials were Yttrium, Lanthanum, Lanthanum/Gadolinium, 620 Nitrate, 630 Nitrate, Zinc Sulfide UV (Green), Bismuth, and Zinc Sulfide UV (Blue). From the University of Louisiana, Lafayette, three Europium Tetrakis powders and two Magnesium Tetrakis powders were acquired (Fontenot et al, 2012; 2015). Sylgard 184 was used as the encapsulation elastomer.

## **Procedures**

The same general procedure was followed for the majority of the composites. First, Sylgard 184 and the curing agent were mixed at a ratio of ten to one to form PDMS. This ratio was predetermined by previous experiments. Following this, the sample was outgassed for four to five minutes. The PDMS was mixed with the phosphor powder at a ratio of twenty-two to one and mixed by hand thoroughly for three to four minutes. The sample was outgassed a second time for four to five minutes. Within the next three to four minutes, the mixture was poured into the dog bone mold and outgassed completely. Lastly, it was cured in an oven at 100 °C for an hour, cooled, and removed from the mold. Aside from this synthesis method, the Europium Tetrakis was

ground from crystals into a powder. As for Bismuth, an eighty-micrometer sieve was utilized to acquire a more homogeneous powder size.

To measure the photoluminescence of the powders, a 405-nanometer laser was first used to excite the electrons. A PDMS layer of 6.26-millimeter thickness was placed on top of the powders. The function generator was set with a square wave at a 1.5 millisecond pulse. A photomultiplier was placed to detect the luminescence of the powders. A variety of lenses were used in order to determine the temperature dependent bandwidths. The stage was connected to the temperature controller in order to vary the temperature of the powders. The powders were given five minutes to rise to the desired temperature if the temperature increment was five degrees Celsius, and eight minutes if the increment was ten degrees Celsius. The photomultiplier was then output into an oscilloscope in order to see the decay of the photoluminescence. From there, the decay rate of each of the powders at elevated temperatures were determined.

The exact same procedures were utilized to determine the decay rates of the composites. One exception is for the Zinc Sulfide UV (Green) for both the powder and composite form: a pulse length of 2.0 millisecond pulse length was utilized since it took the powders longer to reach a steady excited state. For the phosphors with the decay rates that were analyzable at room temperature, they were tested from room temperature to 200 degrees Celsius in five- or ten-degree increments.

## **Results**

For the majority of the phosphor powders, they were successfully encapsulated into PDMS. Table 1 displays which materials were cured successfully and which were not. Other methods of curing were also tested on the Lanthanum/Gadolinium samples such as curing at 200 degrees Celsius and using UV curing. Unfortunately, neither of these methods worked. The composites remained liquid, indicating the powders were interfering with the curing chemical reaction. For the successfully cured samples, the physical characteristics of each composite varied and should be investigated at a later date.

Phosphor Powder	Successful Curing?
1: Yttrium	Yes
2: Lanthanum	Yes
3: Lanthanum/Gadolinium	No
4: 620 Nitrate	Yes
5: 630 Nitrate	Yes
6: Zinc Sulfide UV (Green)	Yes
7: Bismuth	No
8: Zinc Sulfide UV (Blue)	Yes
B: Europium Tetrakis #1	Yes
C: Europium Tetrakis #2	Yes
D: Europium Tetrakis #3	Yes
F: Magnesium Tetrakis #1	Yes
G: Magnesium Tetrakis #2	Yes

**Table 1.** Curing Composites

Next, the optimal wavelengths for each phosphor were observed and recorded. Table 2 shows which wavelength lens should be used for each phosphor.

<b>Phosphor Powder</b>	<b>Optimal Wavelength</b>
1: Yttrium	460 nm
2: Lanthanum	460 nm
3: Lanthanum/Gadolinium	460 nm
4: 620 Nitrate	650 nm
5: 630 Nitrate	650 nm
6: Zinc Sulfide UV (Green)	540 nm
7: Bismuth	540 nm
8: Zinc Sulfide UV (Blue)	460 nm
B: Europium Tetrakis #1	650 nm
C: Europium Tetrakis #2	650 nm
D: Europium Tetrakis #3	650 nm
F: Magnesium Tetrakis #1	460 nm
G: Magnesium Tetrakis #2	460 nm

**Table 2.** Powders and Composites Optimal Wavelength

The optimal wavelength was determined by selecting the most prevalent and analyzable decay rates. An example can be seen in Figure 1.

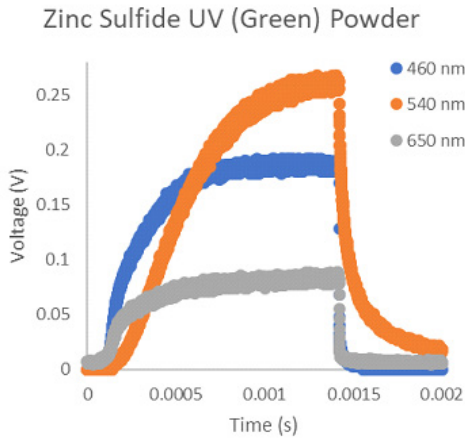


**Figure 1.** The decay rate for Zinc Sulfide UV (Green) Powder is shown above. It displays the amount of voltage against time.

From the figure above, it can be determined that the optimal wavelength for Zinc Sulfide UV (Green) is 540 nm due to the longer decay time. In addition, both the powders and the phosphors had the same optimal wavelengths. This is evident in Figure 2.

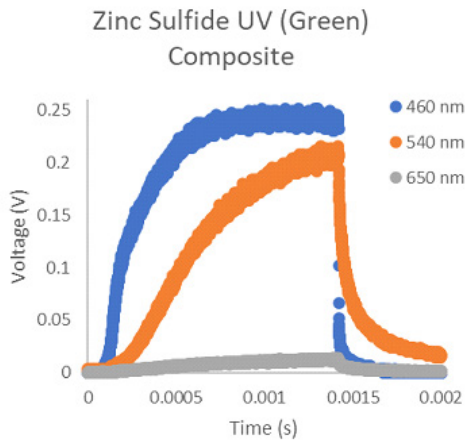


**Figure 2.** The decay rate for Zinc Sulfide UV (Green) Composite. It displays the amount of voltage against time.

Lastly, when setting up the decay behavior of the photo luminescence against the natural logarithm of the temperature, the same linear lines were evident between the powders and their respective composites. The standard data is seen in Figure 3.

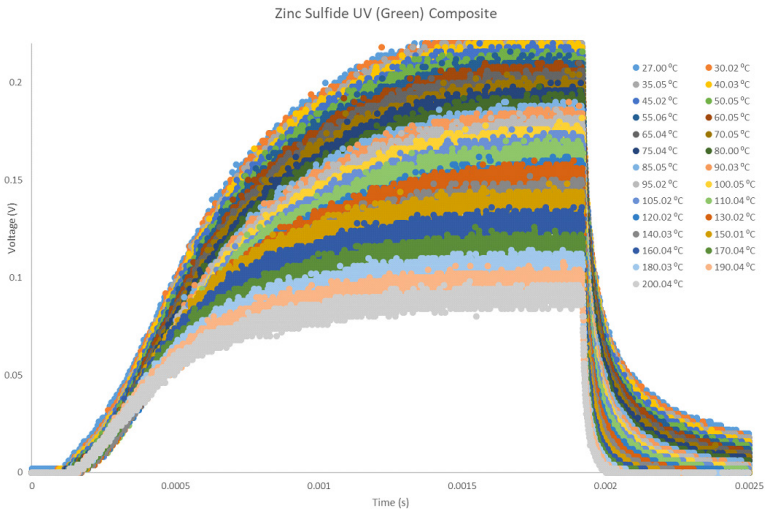


**Figure 3.** The decay rates for various elevated temperatures for Zinc Sulfide UV (Green) Composite using a 540-nanometer wavelength lens. A look at the data shows that higher temperatures are correlated with shorter decay rates.

When plotted in a log plot, the linearity of the correlation can be seen.

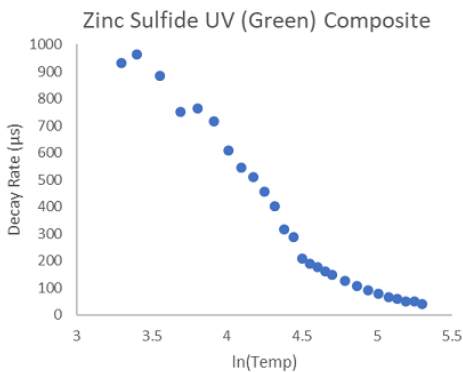


**Figure 4.** The decay rates plotted against the natural logarithm of the temperature. This is for the Zinc Sulfide UV (Green) Composite.

There also appears to be two separate linear sections in the correlation, which should be investigated at a further date. The Zinc powder and the Europium Tetrakis samples were also measured and a linear correlation is also seen. All of the other composites' decay rates were too short to measure at elevated temperatures.

## **Conclusion**

The majority of the powders were successfully encapsulated by PDMS into composite form. In addition, the encapsulation process does not affect the readings on the decay rates. As a result, the benefits of the phosphor powders are retained while the weaknesses are eliminated. With the optimal wavelengths analyzed, the correct lens can be chosen to observe each phosphor powder.

As the composites have been analyzed, the phosphor samples can be used as a temperature sensing apparatus. The composites can be utilized where traditional methods of thermometry are lacking. Since taking readings is non-contact, accurate, and quick, this form of thermometry has many advantages, and one of the best utilizations is in space applications where conditions make temperature readings difficult.

In the future, it would be desirable to see lower temperatures explored. In addition, other characteristic tests of the composites would be useful, as while the effects of PDMS on the powders have been observed to an extent, the effects on the characteristics of PDMS has not. The potential of temperature flux has not been analyzed. It can be achieved by layering the different composites on top of each other and reading the different decay rates. Finally, encapsulation of the powders in other materials such as aerogels would be useful for future study.

## References

- Allison, S. W., Baker, E. S., Lynch, K. J., & Sabri, F. (2017). In vivo X-Ray excited optical luminescence from phosphor-doped aerogel and Sylgard 184 composites. *Radiation Physics and Chemistry*, *135*, 88–93. doi: 10.1016/j.radphyschem.2017.01.045
- Fontenot, R. S., Bhat, K. N., Hollerman, W. A., Aggarwal, M. D., & Nguyen, K. M. (2012). Comparison of the triboluminescent yield and decay time for europium dibenzoylmethide triethylammonium synthesized using different solvents. *CrystEngComm*, *14*(4), 1382–1386. doi: 10.1039/c2ce06277a
- Fontenot, R. S., Owens, C. A., Bhat, K. N., Hollerman, W. A., & Aggarwal, M. D. (2015). Magnesium tetrakis dibenzoylmethide triethylammonium: A novel blue emitting phosphor. *Materials Letters*, *146*, 9–11. doi: 10.1016/j.matlet.2015.01.141
- Fontenot, R. S., Allison, S. W., Lynch, K. J., Hollerman, W. A., & Sabri, F. (2016). Mechanical, spectral, and luminescence properties of ZnS:Mn doped PDMS. *Journal of Luminescence*, *170*, 194–199. doi: 10.1016/j.jlumin.2015.10.047
- Rietema, K. (1991). *The Dynamics of Fine Powders*. Elsevier Applied Science.
- Aryal, M. (2018). Heat flux calculations of PDMS and silica aerogel through phosphor thermometry. [Master thesis, University of Memphis]